

A mobile high spatial-resolution Muography hodoscope based on large-area Micromegas detectors

Yu Wang,^{1,2} Shubin Liu*,^{1,2,3} Zhihang Yao,^{1,3} Yulin Liu,^{1,2} Zhiyong Zhang,^{1,2} Zhengyang He,^{1,2} Ziwen Pan,^{1,2} and Changqing Feng^{1,2}

¹⁾*State Key Laboratory of Particle Detection and Electronics, University of Science and Technology of China, Hefei 230026, China*

²⁾*Department of Modern Physics, University of Science and Technology of China, Hefei 230026, China*

³⁾*School of Nuclear Science and Technology, University of Science and Technology of China, Hefei 230026, China*

(*Electronic mail: liushb@ustc.edu.cn)

(Dated: 8 August 2025)

Muon radiography is an imaging technique based on muon absorption in matter that allows measurement of internal details in hidden objects or structures. This technique relies on measuring cosmic-ray muons tracks accurately, which reflects the incoming muon flux from both the target object and the open sky. In this paper, we report on the construction of a high spatial resolution muography hodoscope based on Micromegas detectors. Using four layers of 40 cm × 40 cm Micromegas detectors, channel multiplexing circuits, and the versatile readout system, a moveable muography hodoscope named μ STC-R400 was designed and constructed. Results show that the channel multiplexing circuits can resolve hit positions correctly, and the spatial resolution of the detector is approximately 190 μ m. Experiments were conducted at an under-construction subway tunnel and outdoors near a mountain, demonstrating the μ STC-R400's ability to maintain high spatial resolution outside the laboratory and its robustness in harsh environments.

I. INTRODUCTION

Cosmic-ray muon, with its strong penetrating power and no radiation hazards, is an ideal probe for imaging the internal structure of large or well-shielded objects. Currently, muon imaging (muography) primarily employs two principles: radiography and tomography. This research focuses on muon radiography. Muon radiography is based on the attenuation of muon flux as cosmic-ray muons pass through large structures, such as geological formations or man-made architectures. The basic principle is illustrated in Fig. 1, where the muon flux is measured by tracking detectors both toward the object ($I_{\text{object}}(\theta, \phi)$) and the open sky ($I_{\text{open-sky}}(\theta, \phi)$). By calculating the ratio $I_{\text{object}}/I_{\text{open-sky}}$, the transmission ratio of cosmic-ray muons can be determined, which is expressed as follows:

$$T(\theta, \phi) = \frac{N_{\text{object}}(\theta, \phi)}{N_{\text{open-sky}}(\theta, \phi)} = \frac{\int_{E_{\min}(X)}^{\infty} \Phi(\theta, E) dE}{\int_{E_0}^{\infty} \Phi(\theta, E) dE} \quad (1)$$

Here, $\Phi(\theta, E)$ is the differential muon flux, $E_{\min}(X)$ is the minimum energy required for a muon to traverse an object with opacity X , and E_0 represents the minimum energy threshold for muons detected (e.g., determined by detector characteristics or analysis cuts). Opacity X is defined as:

$$X(L) = \int_L \rho(x) dx \quad (2)$$

where L is the path length of muon through the object, and $\rho(x)$ is the density of the object along the muon trajectory (θ, ϕ). Using the relationship between muon energy loss

and traversal length, combined with empirical models of the cosmic-ray energy spectrum, the opacity X for a given direction (θ, ϕ) can be determined. Consequently, the density distribution along the detector's line of sight can be inferred.

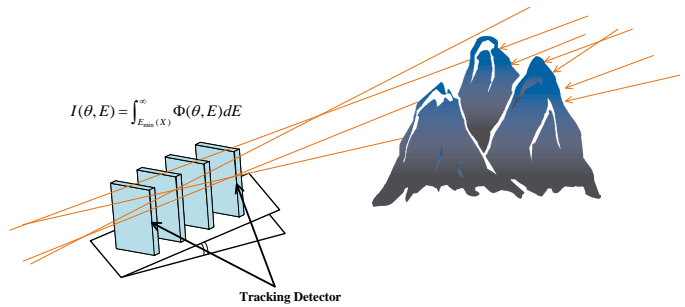


FIG. 1. Principle of muon radiography. Muon flux is measured using a tracking system, typically composed of an array of position-sensitive detectors. Flux attenuation results from muon absorption and scattering as they pass through the object. The attenuation level correlates directly with the object's opacity.

The first application of muon radiography was the measurement of the overburden mass of the Guthega-Munyang tunnel using a Geiger counter array as the sensitive detectors¹. Subsequently, in the 1960s, L.W. Alvarez explored the possibility of searching for hidden chambers within the Second Pyramid of Giza². Over the past three decades, lots of experiments have been conducted in the areas such as volcano image, geological surveying and detection of cavities for archaeological and civil engineering applications³. A notable recent example is the discovery of a big void in Khufu's Pyramid with the combination of nuclear emulsion chambers, plastic scintillator detectors and Micromegas detectors⁴.

The key aspect of muography is the accurate measurement of muon tracks. Except the nuclear emulsion chambers, most detection methods employ multiple layers of detectors to reconstruct these tracks. The use of finer resolution detectors can obtain more accurate results and contribute to a more compact design. Spatial resolution and detection area are two critical parameters for optimizing imaging time and accuracy. Imaging time is determined by the number of muons that penetrate the object and are subsequently recorded by the detectors. A muography facility with a larger detector area has a greater acceptance, allowing the detection of muons from a wider range of directions, which helps to maintain a reasonable experimental duration.

The most common detector type employed in muography is the scintillator with Silicon Photomultiplier (SiPM) readout. A typical scintillator telescope consists of two or more double layers of orthogonal plastic scintillator bars, used to measure muons tracks in two independent projection directions. For rectangular bars, a single muon typically produce hit in one scintillator bar, and the spatial resolution σ is related to the bar's lateral width L , specifically $\sigma = L/\sqrt{12}$. For triangular-shaped bars, spatial resolution can be improved by measuring the signal fraction in adjacent bars, achieving approximately 3 mm for a bar with 1.7 cm high and 3.3 cm wide⁵.

With advancements in nuclear instrumentation, micro-pattern gaseous detectors (MPGDs) have become a feasible option for muon radiography applications, as demonstrated by their uses in imaging Khufu's Pyramid and WatTo experiment⁶. These detectors can achieve a resolution of a few hundred micrometers at a reasonable cost. In particular, the Micromegas (Micro-MEsh Gaseous Structure) detector can achieve a spatial resolution of approximately 100 μm over active areas of thousands of square centimeters. However, a large detection area combined with fine spatial resolution increases the complexity of the readout system design. This challenge can be mitigated through specially designed channel multiplexing methods, achieving a balance between detection area and readout complexity⁷⁻¹¹. On the other hand, gaseous detectors are often considered less suitable for field applications outside the laboratory due to their requirement for a continuous gas supply and their susceptibility to discharge caused by environmental factors such as vapor or dust pollution. These issues can be addressed by carefully controlling the gas flow and by robustly enclosing the detectors.

In this paper, a high spatial-resolution muon radiography hodoscope based on thermal-bonding Micromegas detectors is developed and presented. The sensitive area of this detector is 40 cm \times 40 cm, and the number of anode strips is 2000 for a single detector. To reduce the overall size of the facility, a channel multiplexing method, together with a highly integrated front-end electronics card, is applied in this facility.

This detector achieves a spatial resolution better than 200 μm with the implemented multiplexing circuit and front-end electronics. Subsequently, we performed muon radiography experiments in a subway tunnel under construction, and an outdoor environment near a mountain, demonstrating the capability and stability of this facility.

II. SYSTEM DESIGN AND EXPERIMENTAL SETUP

The muography facility consists of four layers of Micromegas detectors serving as sensitive elements, channel multiplexing circuits to reduce readout electronics requirements, Front-end Electronics Cards (FECs) for signal amplification and digitization, and back-end electronics for event identification and data concentration.

A. Resistive Micromegas Detector

The Micromegas detector is a typical micro-pattern gaseous detector operating in proportional mode, featuring a drift region and a thin amplification gap structure. A simplified cross-sectional structure of the Micromegas is shown in Fig. 2. The active volume is separated into a drift region, where incident particle ionizes the working gas, and an amplification gap, where the primary ionizations are multiplied through the avalanche process.

The distance between the drift cathode and mesh electrode of our detector is 5 mm, and the thickness of the amplification gap is approximately 100 μm . A germanium layer coated on the surface of the anode PCB (Printed Circuit Board) serves as a resistive anode and is connected to the GND of high voltage. The conversion-drift electric field is established by applying negative voltages to the mesh electrode and a slightly higher voltage to the drift cathode.

When a muon enters the detector, primary ionization is generated. The strong electric field in the amplification region draws the primary electrons through the mesh voids and initiates the avalanche process. The ions are then mostly collected by the micro-mesh, and their movement induces the majority of the signal on the readout strips.

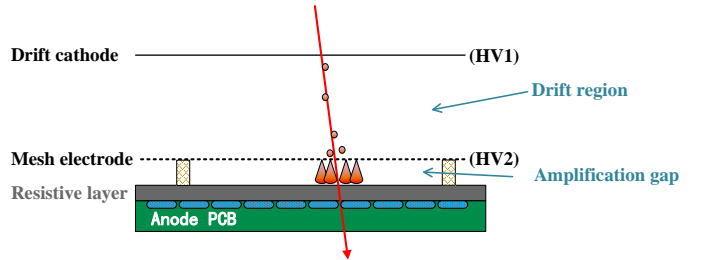


FIG. 2. Simplified cross-sectional structure of the Micromegas detector¹². Note that the thicknesses of the drift region and the amplification gap are not drawn to scale.

As shown in Fig. 3, the readout strips were designed in the second and third layers of the PCB with an orthogonal arrangement. This design makes a single active volume to measure both X and Y hit positions. The strip pitch is 400 μm , with the width of strips in the upper layer being 68 μm and those in the lower layer being 295 μm .

Other than the conventional bulk method based on photolithography manufacturing processes, we employed a thermal bonding method in which small spacers made of thermal

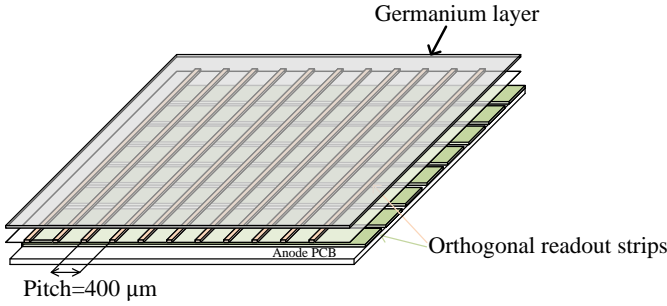


FIG. 3. Structure of the readout strips on the anode PCB, where the second and third layers form the orthogonal readout strips. The germanium layer is coated after PCB manufacture.

bonding film are placed on the anode PCB to support the tensile mesh electrode. Further details about the Micromegas detector can be found in this work¹², where the detector design was enlarged for the present work.

Several detectors with different dimensions were designed and implemented. In this paper, detectors with sensitive areas of $40\text{ cm} \times 40\text{ cm}$ are used to construct the muon hodoscope. A photograph of the Micromegas detector is shown in Fig. 4.

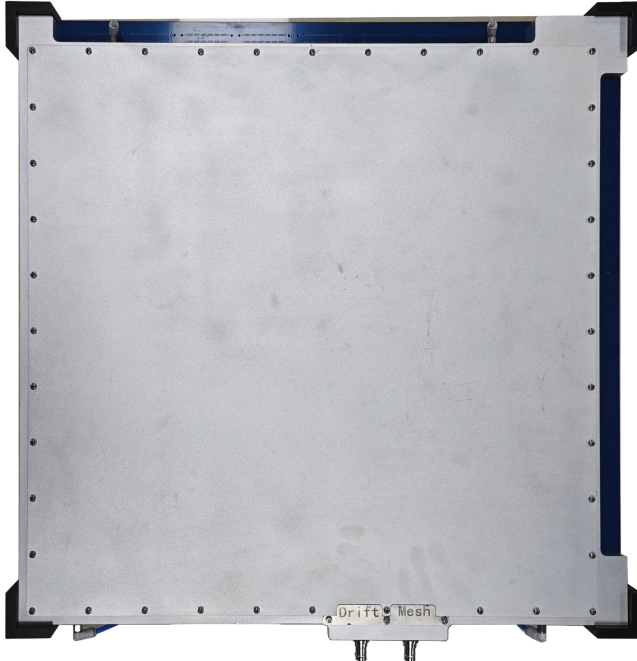


FIG. 4. Photograph of the Micromegas detector ($40\text{ cm} \times 40\text{ cm}$) used in this research.

B. Channel multiplexing Circuit

A major constraint in the application of high-spatial resolution Micromegas detector is the requirement for a large number of readout channels. For example, the detector we used

has 2000 readout channels for the X and Y dimensions combined. For a muon radiography facility with four layers of detectors, the total number of strips requiring readout reaches 8,000. To address this challenge, we proposed a position-encoded multiplexing method, in which each front-end electronics channel reads out multiple detector strips. In this multiplexing approach, the ratio of detector strips to electronics channels is defined as the multiplexing factor.

The fundamental principle of this multiplexing approach is that within a single acquisition window (typically set to a few microseconds or less), at most one muon will hit the detector, and the resulting ionization charges distribute over several adjacent strips near the hit point. Therefore, a specially designed mapping relation can be implemented, where each contiguous strips of the detector are connected to a unique pair of readout electronics channels. When any two readout electronics channels read back signals, multiple possible hit locations could be deduced. However, according to the mapping relationship, only one result corresponds to contiguous strips, which is the actual hit location on the detector. A mathematical model for this approach was established in our previous work, where different types of multiplexing circuits were designed and evaluated¹¹.

In this work, we employ a circuit with a multiplexing factor of eight, where 512 detector strips are multiplexed into 64 front-end electronics channels. The encoding circuit is shown in Fig. 5. For each dimension of the detector strips, two multiplexing circuits are used, meaning that 1024 strips of the detector are read out by 128 channels of electronics.

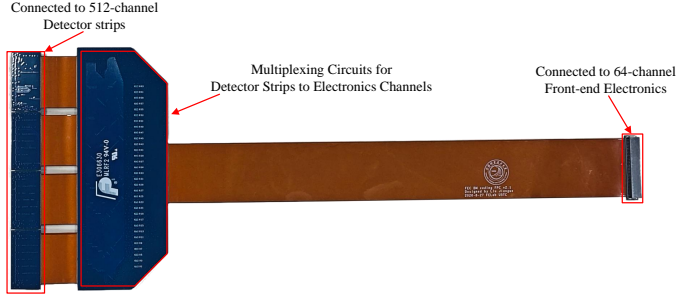


FIG. 5. Photograph of the multiplexing circuit that connects 512 detector strips to 64 readout electronics channels.

C. Front-end Electronics Card (FEC)

The readout is handled by an FEC which adopts a design that was verified in the PandaX III (Particle AND Astrophysical Xenon experiment III) project¹³. The key differences lie in the use of an upgraded version of the readout ASIC named STAGE (SEcond stAGE of the AGET^{14,15}) and the utilization of channel hit information for self-trigger signal generation.

The structure of the STAGE chip is shown in Fig. 6. It has 64 active channels which process the signals from the Micromegas detector after channel multiplexing, and 4 dummy channels which are not connected to the detector but serve

as noise monitors for the chip. Each channel consists of a charge sensitive amplifier (CSA), a pole-zero canceller (PZC), an analog shaper, a discriminator for trigger generation, and a 512-cell switched capacitor array (SCA). The amplified and shaped signal is sampled by the SCA and then sent out of the chip under the control of the field-programmable gate array (FPGA) on the FEC. The trigger signal from each channel contributes to the total trigger signal, with the amplitude proportional to the number of channels exceeding the on-chip threshold.

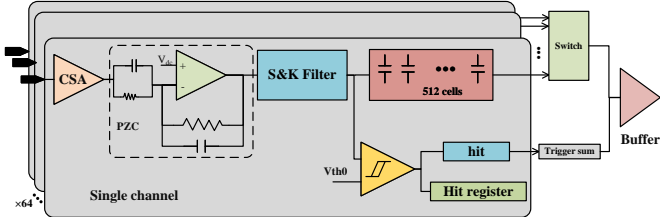


FIG. 6. Block diagram of the STAGE chip. Modified from this work¹⁵.

A single FEC uses four STAGE chips to sample the encoded signals, with one FEC reading out exactly one layer of the detector. The output of each STAGE chip is digitized by a single-channel 12-bit analog-to-digital converter (ADC) and processed by the FPGA. A channel-specific threshold is set to suppress the idle channels. All digitized data with values greater than the preset thresholds, along with timestamp, trigger number, and checksum, are constructed into a user-defined data frame and transmitted to the back-end data acquisition (DAQ) board.

D. Back-end Electronics and Remote Control

A back-end electronics card designed for small to medium-scale physics experiments is adopted in the construction of this muography facility¹⁶. It performs data gathering from the FECs, event identification of potential muons, and data transmission to the host PC.

The back-end electronics card communicates with the FECs via optical fiber interfaces using a custom-defined protocol. With the time domain multiplexing (TDM) method, the link between the back-end electronics and FECs is divided into three virtual channels for trigger, data, and command transmission.

For remote control, a 4G modem provides internet access to the facility. A Windows Subsystem for Linux (WSL) based automatic data processing procedure performs data processing and transmission to the laboratory server. Manual control, remote debugging, and testing are performed via Windows Remote Desktop through a ZeroTier network.

E. Self-trigger mode

A self-trigger mode was developed to select potential muon signals while the facility operates in continuous mode. This mode consists of two parts: pre-signals generated by the FECs indicating that over-threshold signals have been detected, and valid triggers generated by the back-end electronics after performing trigger selection.

The pre-trigger signal is generated through two stages in the FEC. The first stage is implemented using the built-in ‘multiplicity’ function of the ASIC¹⁵. As shown in Fig. 6, during the acquisition phase, the shaped signal is continuously sampled by the SCA and simultaneously compared with a programmable voltage threshold. If the signal exceeds the threshold, a single-channel hit signal is generated. A total trigger signal is then produced based on the single-channel hit signals in an analog mode, with an amplitude proportional to the number of single-channel hits. This total trigger signal is amplified to the differential analog output ports and continuously acquired by the on-board ADC. A second-stage threshold is applied to identify valid multiplicity signals. Two thresholds are implemented in the FPGA: a lower one to suppress triggers caused by noise, and a higher one to eliminate spurious triggers resulting from discharges in the Micromegas detectors. When a potential event is detected, the FEC sends a pre-trigger signal to the back-end electronics.

The back-end electronics records pre-trigger signals from each FEC and maintains them for a programmable time period, after which the register is cleared. If the recorded pre-triggers match the configured trigger pattern, a fast trigger signal followed by a 32-bit trigger ID is distributed to all FECs. Upon receiving the fast trigger signal, the FEC stops the acquisition phase and controls the ASICs to sequentially output the sampled analog signals from the SCAs for conversion. The digitized data is compared against the preset channel-specific thresholds, and only data exceeding these thresholds is packaged and transmitted to the back-end electronics.

F. Construction of the Hodoscope

A muon radiography facility was constructed using these detectors and electronics cards, and named μ STC-R400 (muon Scattering and Transmission imaging faCility with 400 mm \times 400 mm detectors used in radiography). As shown in Fig. 7, this radiography facility contains four layers of Micromegas detectors, four FECs, a back-end electronics card, a mini-PC, two high-voltage (HV) modules housed in a mini-NIM case, and a remote-controlled Ackerman chassis to support the entire system. The dip angle and horizontal angle are controlled by two motors, the viewing angle and direction can be adjusted according to the target objects.

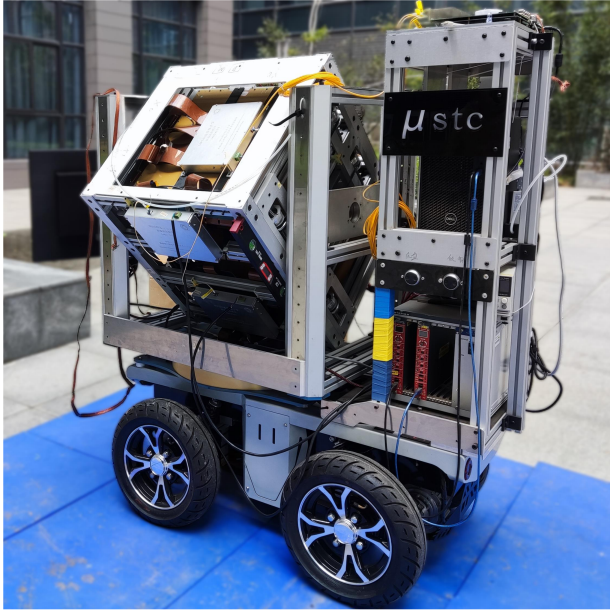


FIG. 7. Photograph of the μ STC-R400. The constructed system includes Micromegas detectors, FECs, back-end electronics card, PC, HV modules, and the four-wheel chassis.

III. EXPERIMENTAL RESULTS

A. Performance of the Readout Electronics

The readout electronics cards were calibrated before installation into the μ STC-R400. In the calibration, a charge signal was generated by applying a step-down voltage through a 1 pF capacitor in series and fed into the calibration pin of the ASICs (In_cal input). With the dynamic range set to 120 fC and a peaking time of 1039 ns, the charge-to-ADC conversion gain is approximately 29 ADC units/fC. Under this calibration relationship, the root mean square (RMS) value of the equivalent noise charge (ENC) for all channels connected to the detector via channel multiplexing circuits is shown in Fig. 8, with 95% of the FEC channels exhibiting noise less than 0.78 fC.

B. Energy Spectrum and Position Decoding

The detectors operate in gas-flow mode, with the working gas being a mixture of argon and 7% carbon dioxide. In our experiments, the gas flow was set to 25 mL/min and the working voltages of the drift cathode and mesh were set to -570 V and -720 V, respectively.

Each cosmic ray muon deposits energy in the drift area, generating ionization. This ionization is avalanche in the amplification gap, generating induction signals on the readout strips in both X- and Y-directions. By summing the charges on the adjacent strips for each valid event, the cosmic ray energy deposition spectrum is obtained and shown in Fig. 9. The charge distribution mainly follows the expected Landau distri-

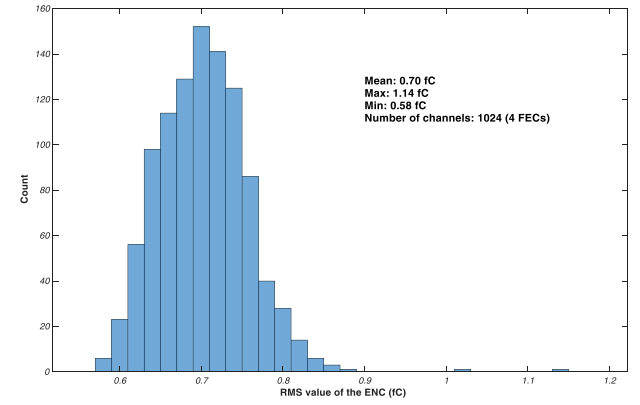


FIG. 8. Distribution of the RMS noise of the FECs connected to the detector.

bution. After performing a Landau–Gaussian convolution fit using ROOT, the peak value is approximately 125 fC.

Since the strips of the detectors are multiplexed, the hit positions can be decoded when more than one readout electronics channel registers valid signals. Figure 10 shows the distribution of the number of channels exceeding thresholds in each event. This result indicates that the position encoding multiplexing method can achieve nearly lossless channel compression in this muography facility.

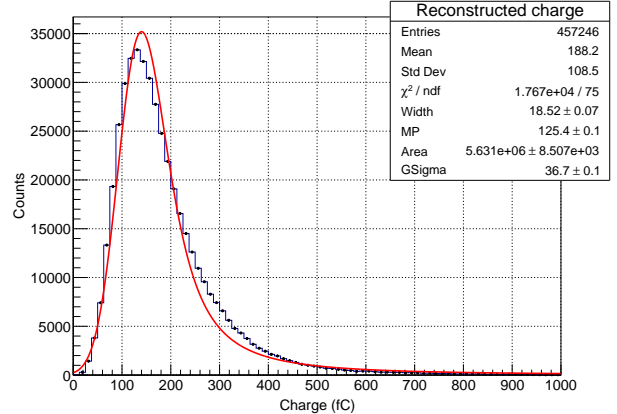


FIG. 9. Energy deposition spectrum of cosmic ray muons measured by the detector.

C. Spatial Resolution Result

The principle of calculating the spatial resolution of a single detector is shown in Fig. 11. Take one of the layer as the target layer, and using the hit positions of the other three layers to fit a reference track. The fitting result can be expressed as $x_{fit} = k_x \times z_t + b_x$, where k_x and b_x are the slope and intercept of the fitting track, respectively, and z_t is the z coordinate of the target layer. After detector alignment to correct the installation offsets and rotations, the deviation $\Delta x = x_{hit} - x_{fit}$

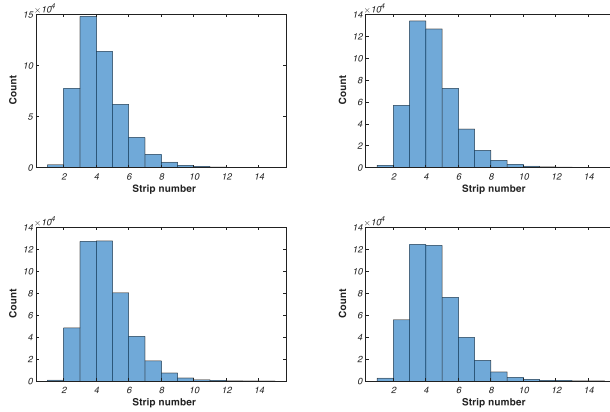


FIG. 10. Distribution of the number of channels exceeding thresholds in each event.

can be calculated, where x_{hit} is the hit position measured by the target detector. By statistics analyzing a large number of muon tracks, the distribution of Δx can be obtained and fitted with a double gauss function. Figure 12 shows the fitting result of the Δx in the X direction of the inner layer detector with incident angle of $0^\circ \sim 5^\circ$. The narrow component or the core Gaussian distribution (blue line) has a standard deviation of 0.188 mm. The spatial resolution was defined as a standard deviation of Δx and divided into two parts: the deviation of trajectory fitting ($\sigma(x_{fit})$) and the residual of the detector under test ($\sigma(x_{hit})$). In the muography applications, these two parts will both contribute to the muon tracks measurement, and it is viewed as the spatial resolution of the facility.

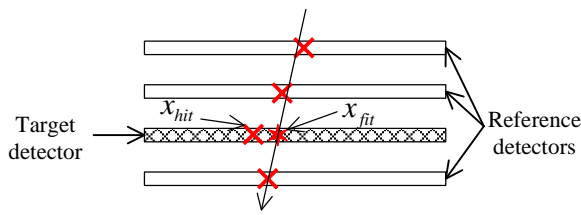


FIG. 11. Illustration of the method for calculating spatial resolution. The actual hit positions are represented by red crosses, while the fit hit position is indicated by a red hexagon.

D. Muon Radiography Experiments Results

1. Measurement at an Underground Tunnel

An experiment was performed at a subway tunnel under construction in the authors' city. As shown in Fig. 13, the μ STC-R400 was placed in the subway tunnel approximately 18 m below the ground surface. A river on the ground flows above the subway tunnel, approximately perpendicular to it. According to the engineering investigation, the vertical distance between the riverbed and the bottom of the tunnel is

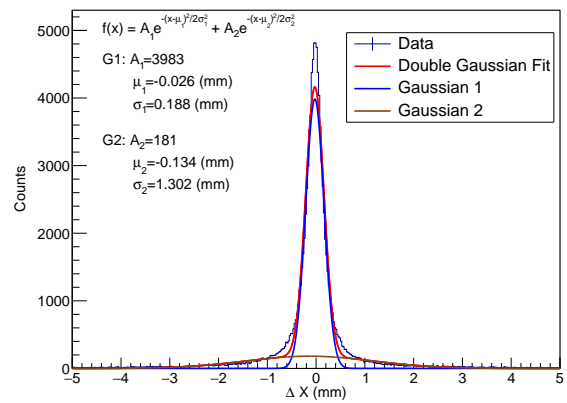


FIG. 12. Deviation distributions of the Micromegas in the X directions with incident angle of $0^\circ \sim 5^\circ$.

about 11 m. Since the subway site was under construction during the experiment, a UPS module was used to prevent power surges and sudden power loss. Remote control was implemented via the local WiFi network in the tunnel for monitoring the status of detectors and readout electronics.

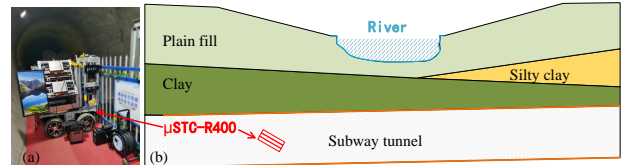


FIG. 13. (a) Placement of the detector in the underground tunnel and the cross-section of the stratum from engineering investigation; (b) Photograph of the μ STC-R400 facility in the under-construction subway tunnel with a dip angle of 30° and oriented toward the river on the ground surface. The direction of the river is approximately perpendicular to the subway tunnel.

The measurement in the tunnel lasted approximately 300 hours, while an open-sky muon flux measurement conducted at ground level on the USTC campus lasted about 266 hours. After performing position alignment to correct offset and rotation errors, muon tracks were reconstructed where all 4 layers of detectors were fired and the RMSE of the fitted tracks was less than 2 mm. Figure 14 shows the 2D hit distributions measured on the ground and in the tunnel, with counts normalized to one hour. Figure 15 shows the distributions of the θ and ϕ angles for open-sky and tunnel measurements (counts normalized to one hour). Results show that the muon flux is attenuated by the soil above the tunnel, while the influence of the river is not significant. Nonetheless, the μ STC-R400 has demonstrated its robustness by operating successfully in the subway tunnel environment where vapor and dust were present during the test.

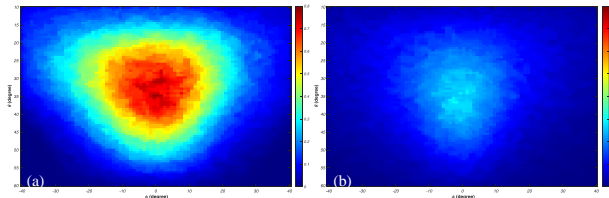


FIG. 14. (a) 2D hit distribution for open-sky measurements; (b) 2D hit distribution measured in the tunnel.

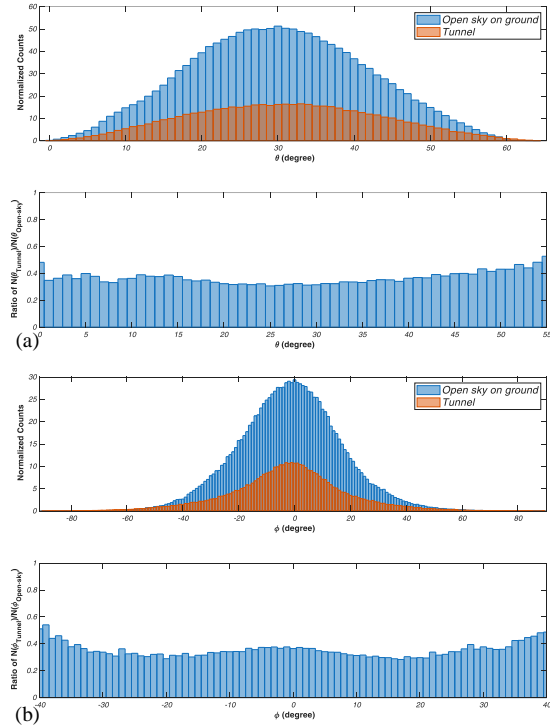


FIG. 15. (a) Distribution of the θ angle and the ratio $\theta(N_{\text{tunnel}})/\theta(N_{\text{open-sky}})$; (b) Distribution of the ϕ angle and the ratio $\phi(N_{\text{tunnel}})/\phi(N_{\text{open-sky}})$.

2. Measurement at a Mountain

To validate the versatility of this muography facility in outdoor environments, an experiment was performed at Dashu Mountain in the Shushan Forest Park located in the urban area of Hefei. As shown in Fig. 16(a) and (b), the μ STC-R400 was placed in a microbus positioned near the foot of the mountain. The horizontal distance between the facility and the top of Dashu Mountain is approximately 1 km, with a vertical distance of about 200 m. To measure both the open-sky muon flux and the flux through the mountain at the same time, the detectors were rotated so that their normal was parallel to the ground, with the center approximately pointing toward the mountain peak. As shown in Fig. 16(c), the detectors could simultaneously record muons from both the mountain direction and the open sky. This configuration ensured that fluctuations in muon flux and detector gain remained equal for both the target measurement and the background measurement.

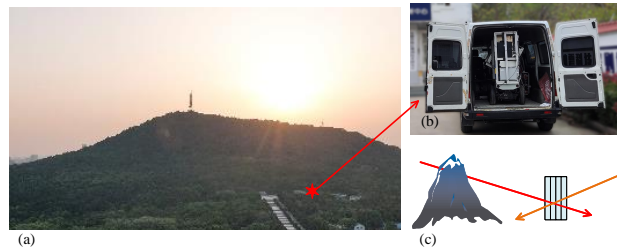


FIG. 16. (a) View of Dashu Mountain, with the μ STC-R400 placed at the foot of the mountain (approximately at the location marked by the hexagram); (b) Photograph of the facility placed in a microbus; (c) Diagram of the detector placement, where the normal of the detector is parallel to the ground.

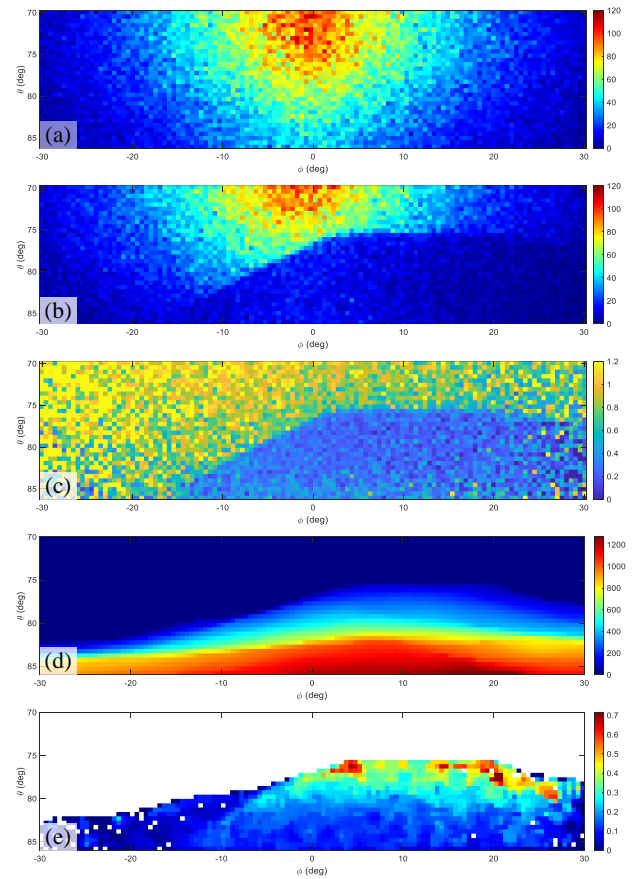


FIG. 17. (a) 2D hit distribution from the open-sky direction; (b) 2D hit distribution from the mountain direction; (c) Transmission ratio calculated as $N_{\text{mountain}}/N_{\text{open-sky}}$ with values larger than 1.2 set to 1.2; (d) Traversed length from the experiment site perspective; (e) Reconstructed density using a constant minimum transmission energy of $2.5 \text{ MeV} \cdot \text{g}^{-1} \cdot \text{cm}^2 \cdot X$.

The test continued for approximately 37 days, during which a heavy snowfall occurred in Hefei, yet the facility maintained proper functioning. The 2D distribution of muons from the open-sky direction and from the mountain direction is shown in Fig. 17(a) and (b), where the 'shadow' caused by the mountain's absorption is clearly visible. Figure 17(c) shows the

transmission ratio, where values larger than 1.2 were set to 1.2 to provide a clear color gradation. The shape of Dashu Mountain was obtained through drone mapping with an accuracy of 10 m, and Fig. 17(d) shows the traversal length at the experiment site.

With the known transmission rate $T(\theta, \phi)$, the traversal length $L(\theta, \phi)$, and according to (1), the average density of the object can be calculated as $\bar{\rho}(\theta, \phi) = X(\theta, \phi | X_{\min}) / L(\theta, \phi)$, where $X(\theta, \phi | X_{\min})$ is the minimum energy required to traverse the objects. The reconstructed density is shown in Fig. 17(e) using parameters from the Eco-Mug library¹⁷ and from this work¹⁸, with the mountain body treated as rock with $E_{\min} = 2.5 \text{ MeV} \cdot \text{g}^{-1} \cdot \text{cm}^2 \times X$. The reconstructed density values are lower than expected empirical values, possibly due to uncertainties in X_{\min} at large incident angles and in the traversal length.

IV. DISCUSSION AND CONCLUSIONS

In this study, a high spatial resolution muon radiography facility named μ STC-R400 was designed and implemented. Four layers of detectors with a sensitive area of $40 \text{ cm} \times 40 \text{ cm}$ were used, requiring a total of 8000 strips to be read out. A channel multiplexing method was applied to reduce the large number of readout channels. Together with the scalable readout system and the self-trigger mode, this facility could be constructed in a relatively compact size. Test results show that the RMS of the ENC is approximately 0.8 fC with a dynamic range of $0 \sim 120 \text{ fC}$, which adequately covers the signal range of the Micromegas detector. The spatial resolution of the detectors with encoding readout is approximately $190 \mu\text{m}$, which provides sufficient tracking resolution for muon radiography. The long-term stability and environmental suitability were tested during different types of experiments in harsh environments, demonstrating that with proper design and sealing, the Micromegas detectors can operate effectively in muography experiments outside the laboratory. The facility presented in this article indicates that Micromegas detectors with the thermal bonding method can be a promising solution for building high spatial resolution muography facilities, while the channel multiplexing readout circuit significantly reduces system complexity. Current research and development efforts are ongoing toward further enhancement of the facility. In the future, more algorithms can be developed based on the high-resolution muon track data.

ACKNOWLEDGMENTS

This work was financially supported in part by the National Natural Science Foundation of China (NSFC) for Distinguished Young Scholars under Grant No. 12025504, in part by the National Natural Science Foundation of China (NSFC) for Young Scientists under Grant No. 12205297, and in part by the University of Science and Technology of China.

The authors would like to express their sincere gratitude to Yong Zhou, Sicheng Wen, Han Han, Xing Xu, Haibin Fei,

Bo Wang, Mujun Li, Jiale Gao, and Xiaozhao Cao from Jianwei Scientific Instruments (Anhui) Technology Co., Ltd. for their help in detector manufacturing, facility construction and experiments deployment.

The authors also extend their appreciation to China Construction Eighth Engineering Division CORP., LTD. for their assistance with the experimental site in the subway tunnel.

The authors are grateful to Haigang Zheng, Hongbo Sun, and Xiao Liang from Anhui Earthquake Agency for their support at the Dashu Mountain experimental site.

DATA AVAILABILITY STATEMENT

The data that support the findings of this study are available from the first author and the corresponding author upon reasonable request.

REFERENCES

- ¹E. GEORGE, Commonwealth Engineer , 445–447 (1955).
- ²L. W. Alvarez, J. A. Anderson, F. E. Bedwei, J. Burkhard, A. Fakhry, A. Girgis, A. Goneid, F. Hassan, D. Iverson, G. Lynch, Z. Miligy, A. H. Moussa, M. Sharkawi, and L. Yazolino, *Science* **167**, 832 (1970).
- ³P. Scampoli and A. Ariga, eds., *Cosmic Ray Muography* (World Scientific Publishing Company, 2023).
- ⁴K. Morishima, M. Kuno, A. Nishio, N. Kitagawa, Y. Manabe, M. Moto, F. Takasaki, H. Fujii, K. Satoh, H. Kodama, K. Hayashi, S. Odaka, S. Procureur, D. Attié, S. Bouteille, D. Calvet, C. Filosa, P. Magnier, I. Mandjavidze, M. Riallot, B. Marini, P. Gable, Y. Date, M. Sugiura, Y. Elshayeb, T. Elnady, M. Ezzy, E. Guerriero, V. Steiger, N. Serikoff, J.-B. Mouret, B. Charlès, H. Helal, and M. Tayoubi, *Nature* **552**, 386–390 (2017).
- ⁵M. D'Errico, F. Ambrosino, G. Baccani, L. Bonechi, M. Bongi, A. Bross, R. Ciaranfi, L. Cimmino, V. Ciulli, R. D'Alessandro, F. Giudicepietro, S. Gonzi, G. Macedonio, V. Masone, B. Melon, N. Mori, M. Orazi, G. Passeggi, R. Peluso, A. Pla-Dalmau, G. Saracino, G. Scarpati, P. Strolin, E. Vertechi, and L. Viliani, *Journal of Physics: Conference Series* **2374**, 012190 (2022).
- ⁶S. Bouteille, D. Attié, P. Baron, D. Calvet, P. Magnier, I. Mandjavidze, S. Procureur, M. Riallot, and M. Winkler, *Nuclear Instruments and Methods in Physics Research Section A: Accelerators, Spectrometers, Detectors and Associated Equipment* **834**, 223 (2016).
- ⁷S. Procureur, R. Dupré, and S. Aune, *Nuclear Instruments and Methods in Physics Research Section A: Accelerators, Spectrometers, Detectors and Associated Equipment* **729**, 888 (2013).
- ⁸B. Qi, S. Liu, H. Ji, Z. Shen, S. Ma, H. Liu, W. Huang, and Q. An, *Chinese Physics C* **40**, 056102 (2016).
- ⁹S. Bouteille, D. Attié, P. Baron, D. Calvet, P. Magnier, I. Mandjavidze, S. Procureur, and M. Riallot, *Nuclear Instruments and Methods in Physics Research Section A: Accelerators, Spectrometers, Detectors and Associated Equipment* **834**, 187 (2016).
- ¹⁰G. Yuan, S. Liu, B. Qi, C. Feng, and S. Ma, *IEEE Transactions on Nuclear Science* **64**, 1346 (2017).
- ¹¹Y. Wang, S. Liu, H. Zhuang, Z. Ding, Z. Yao, C. Feng, and Z. Zhang, *IEEE Transactions on Nuclear Science* **72**, 765 (2025).
- ¹²Jianxin Feng, Zhiyong Zhang, Jianbei Liu, Binbin Qi, Anqi Wang, Ming Shao, and Yi Zhou, *Nuclear Instruments and Methods in Physics Research Section A: Accelerators, Spectrometers, Detectors and Associated Equipment* **989**, 164958 (2021).
- ¹³D. Zhu, S. Liu, C. Feng, C. Li, J. Dong, H. Chen, Z. Chen, and J. Pan, *IEEE Transactions on Nuclear Science* **66**, 1123 (2019).
- ¹⁴S. Anvar, P. Baron, B. Blank, J. Chavas, E. Delagnes, F. Druillole, P. Hellmuth, L. Nalpas, J. L. Pedroza, J. Pibernat, E. Pollacco, A. Rebii, and

N. Usher, in *2011 IEEE Nuclear Science Symposium Conference Record* (2011) pp. 745–749.

¹⁵D. Baudin, D. Attié, P. Baron, D. Bernard, D. Calvet, A. Delbart, Y. Geerbaert, and P. Gros, *Nuclear Instruments and Methods in Physics Research Section A: Accelerators, Spectrometers, Detectors and Associated Equipment New Developments In Photodetection 2017*, **912**, 66 (2018).

¹⁶J. Liu, Y. Wang, C. Feng, S. Liu, and Q. Chen, *Journal of Instrumentation* **20**, T05002 (2025).

¹⁷D. Pagano, G. Bonomi, A. Donzella, A. Zenoni, G. Zumerle, and N. Zurlo, *Nuclear Instruments and Methods in Physics Research Section A: Accelerators, Spectrometers, Detectors and Associated Equipment* **1014**, 165732 (2021).

¹⁸J. Marteau, J. d. B. d'Ars, D. Gibert, K. Jourde, J.-C. Ianigro, and B. Carlus, *Journal of Instrumentation* **12**, C02008 (2017).